Appl. Phys. B (2015) 120:185–199
DOI 10.1007/s00340-015-6167-0

Applied Physics B
Lasers and Optics

RAPID COMMUNICATION

Infrared planar laser-induced fluorescence with a CW quantum-cascade laser for spatially resolved CO_2 and gas properties

Christopher S. Goldenstein[1] · Victor A. Miller[1] · Ronald K. Hanson[1]

Received: 18 March 2015 / Accepted: 30 June 2015 / Published online: 19 July 2015

Abstract The design and demonstration of a new infrared laser-induced fluorescence (IR-LIF) technique that enables spatially resolved measurements of CO_2, temperature, and pressure, with potential for velocity, are presented. A continuous-wave, wavelength-tunable, quantum-cascade laser (QCL) near 4.3 μm with up to 120 mW was used to directly excite the asymmetric-stretch fundamental-vibration band of CO_2 for approximately 200 to 10^5 times more absorbance compared with previous IR-LIF techniques. This enabled LIF detection limits (signal-to-noise ratio of 1) of 20 and 70 ppm of CO_2 in Ar and N_2, respectively, at 1 bar and 296 K in static-cell experiments. Simplified and detailed kinetic models for simulating the LIF signal as a function of gas properties are presented and enable quantitative, calibration-free, IR-LIF measurements of CO_2 mole fraction within 1–8 % of known values at 0.5–1 bar. By scanning the laser across two absorption transitions and performing a multi-line Voigt fit to the LIF signal, measurements of temperature, pressure, and χ_{CO_2} within 2 % of known values were obtained. LIF measurements of gas pressure at a repetition rate up to 200 Hz (in argon) are also presented. Planar-LIF (PLIF) was used to image steady and unsteady CO_2–Ar jets at 330 frames per second with a spatial signal-to-noise ratio (SNR) up to 25, corresponding to a detection limit (SNR = 1) of 200 ppm with a projected pixel size of 40 μm. The gas pressure was measured within 3 ± 2 % of the known value (1 bar) at 5 Hz by scanning the QCL across the P(42) absorption transition and least-squares fitting a Voigt profile to the PLIF signal. Spatially resolved measurements of absolute CO_2 mole fraction in a laminar jet are also presented.

Keywords Laser-induced fluorescence · Quantum-cascade laser · Infrared photophysics · CO_2

✉ Christopher S. Goldenstein
csgolden@stanford.edu

[1] High Temperature Gasdynamics Laboratory, Stanford University, Stanford, CA 94305, USA

1 LIF Introduction

Laser-induced fluorescence (LIF) is an established technique for spatially resolved imaging of gas temperature, pressure, velocity, and gaseous species along a laser beam [1–5] or in a laser sheet [6–11]. However, to date the vast majority of LIF and planar-LIF (PLIF) work has been conducted at ultraviolet (UV) and visible (Vis) wavelengths due to the large Einstein A coefficients of electronic transitions and availability of high-power UV and Vis lasers. Tunable continuous-wave (CW) and pulsed lasers have also been used in the UV and Vis to scan across electronic absorption transitions and record absorption lineshapes via LIF; a few notable examples are [1, 2, 4, 10], and a review of diode laser-induced fluorescence can be found in [5].

Despite the relatively small Einstein A coefficients of rovibrational transitions in the infrared, IR-PLIF is an attractive technique due to its potential to image a plethora of molecular species that are not easily accessible in the UV or Vis (e.g., CO, CO_2, H_2O). To date, IR-LIF and IR-PLIF have received limited use and attention in the literature. Kirby and Hanson were the first to demonstrate IR-PLIF, focusing initially on CO [12], CO_2 [13], and saturated PLIF of CO_2 [14], and they were able to achieve impressive results with detection limits near 1000 ppm for CO and CO_2. Rothamer and Hanson [15] later used a similar optical setup to image temperature and pressure in an underexpanded jet using IR-PLIF. In addition, Alwahabi et al. [16]

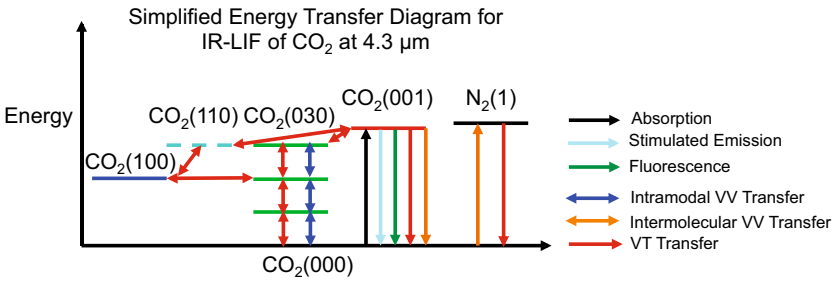

Fig. 1 Simplified energy-level diagram for IR-LIF of CO_2 at 4.3 μm. All states and energy-transfer processes used in the simplified kinetic model are shown here

used scanned-wavelength excitation near 2.0 μm to image CO_2 lineshapes using IR-LIF, and Zetterberg et al. [17] used IR-PLIF of CO_2 with excitation at 2.7 μm to study catalytic oxidation of CO in a harsh environment. These prior works have all relied on the use of high-power, pulsed lasers to excite the fundamental-vibration bands of these species via laser absorption of overtone and combination bands. Li et al. [18] used low-power CW tunable diode lasers near 1.4 μm for IR-LIF of H_2O; however, the extremely small fluorescence signals (order of 10–100 pW) restricted the sensor to pressures below 53 mbar and required beam chopping and a lock-in amplifier to achieve sufficient signal-to-noise ratio at a measurement rate of 0.02 Hz.

To the best of our knowledge, the work presented here represents the first: (1) use of fundamental-vibration-band absorption in IR-LIF and IR-PLIF and (2) demonstration of CW IR-PLIF. A CW, wavelength-tunable, external-cavity quantum-cascade laser (EC-QCL) was used to directly excite the asymmetric-stretch (ν_3) fundamental-vibration band of CO_2 for 200 [17] to 10^5 [14] times more absorbance than previous CO_2-based IR-PLIF techniques. These attributes enabled scanned-wavelength IR-LIF signals with ≈50 times larger SNR (SNR ≈ 250 here with 0.5 % CO_2 at 1 bar in a non-optimized setup) despite ≈10^7 times less laser power compared with previous scanned-wavelength IR-LIF of CO_2 [16]. This technique, with potential for spatially resolved measurements of CO_2, temperature, pressure, and velocity in gaseous flows, is demonstrated here with (1) simultaneous LIF point measurements of temperature, pressure, and CO_2 mole fraction in a static cell with ≈ 0.5 % CO_2 in Ar or N_2 and (2) images of CO_2 mole fraction and pressure in CO_2–Ar jets. PLIF images were acquired at 330 FPS (limited by the camera frame rate) with an exposure time of 100 μs (equivalent to 10 kFPS), which represents a 30× gain in IR-PLIF bandwidth. PLIF measurements are demonstrated with a spatial SNR of 25, and pressure measurements accurate within 3 % of known values (1 bar) were acquired by scanning the QCL across the P(42) absorption transition at 5 Hz. These improvements in SNR and bandwidth coincide with a dramatically simplified experimental setup primarily consisting of a turnkey laser, commercially available lenses, and an IR detector or camera (see Fig. 5). Simplified and detailed kinetic models for simulating the LIF signal as a function of gas properties are presented and enable quantitative, calibration-free, IR-LIF measurements of CO_2 mole fraction within 1–8 % of known values at 0.5–1 bar.

2 Fundamentals of IR laser-induced fluorescence

2.1 Theory

The fundamentals of IR-LIF are presented here to define the units, conventions, and physical processes that are used in the kinetic models presented in Sect. 4.2. Figure 1 shows a simplified energy diagram highlighting the dominant processes and vibrational states (labeled by the vibrational quantum numbers $v_1v_2v_3$) relevant to IR-LIF of CO_2 at 4.3 μm.

The fluorescence signal, ignoring fluorescence trapping, at optical frequency ν in units of W is given by Eq. (1):

$$S_F(\nu) = \text{Incident power} \times \text{fraction absorbed} \times \text{fraction emitted} \times \text{fraction collected} \quad (1)$$

where all quantities are for the volume of gas being imaged and the fractional change in power across the imaged volume is negligible. If laser pumping does not significantly perturb the population in the absorbing state and the imaged volume is optically thin, the *Fraction Absorbed* is given by the spectral absorbance, $\alpha(\nu) = S(T) \times P \times \chi_{\text{Abs}} \times \Phi(\nu) \times L_{\text{imaged}}$ where ν (cm^{-1}) is the optical frequency, $S(T)$ ($\text{cm}^{-2}\,\text{atm}^{-1}$) is the line-strength of the absorption transition at temperature T, P (atm) is the pressure of the gas, χ_{Abs} is the absorbing species mole fraction, Φ (cm) is the lineshape function of the absorption transition, and L_{imaged} (cm) is the length of the gas volume being imaged. A Voigt profile was used to model the lineshape of all spectra. The Voigt profile depends on the Doppler and collisional full width at half maximum given by $\Delta\nu_D = \nu_o 7.1623 \times 10^{-7}\sqrt{T/M}$ and $\Delta\nu_c = 2P\sum_k \gamma_k\chi_k$, respectively. M (g mol^{-1}) is the molecular weight of the absorbing species and γ_k ($\text{cm}^{-1}\text{atm}^{-1}$) is the collisional-broadening coefficient of perturber k. If the absorbing state is perturbed by laser pumping, the *Fraction Absorbed* can be calculated using Eq. (2):

$$\text{Fraction absorbed} = \frac{F_{\text{AbsState}} k_{\text{Abs}}}{\#\text{incident photons/s}} \tag{2}$$

where F_{AbsState} is the fraction of absorbing molecules in the absorbing state and k_{Abs} (s^{-1}) is the rate coefficient for absorption given by Eq. (3).

$$k_{\text{Abs}} = B_{12} I(\nu) \phi(\nu) / c^2 \tag{3}$$

Here, B_{12} is the Einstein B coefficient for the absorption transition related to the Einstein B coefficient for stimulated emission (B_{21}) by Eq. (4), $I(\nu)$ (W cm^{-2}) is the radiation intensity of the laser at ν, and c (cm s^{-1}) is the speed of light.

$$B_{12} = \frac{g_2}{g_1} B_{21} \tag{4}$$

where g_1 and g_2 are the degeneracy of the lower and upper states, respectively. Here, the degeneracy of each state is that of the rotational state (i.e., $2J + 1$). B_{21} can be calculated from the Einstein A coefficient of the rovibrational transition, A_{21} (s^{-1}) (taken from HITRAN 2012 database here [19]).

$$B_{21} = A_{21} \frac{c^3}{8\pi h (\nu c)^3} \tag{5}$$

Here, h (J s) is Planck's constant. The rate coefficient for stimulated emission out of the upper state is given by Eq. (6).

$$k_{\text{Emiss}} = \frac{g_2}{g_1} k_{\text{Abs}} \tag{6}$$

The *fraction emitted* is the fluorescence quantum yield, *FQY*, given by Eq. (7).

$$\text{FQY} = \frac{\sum_{X,Y} (F_{\text{CO}_2,XY1} A_{001\to000} + F_{\text{CO}_2,XY2} A_{002\to001})}{F_{\text{CO}_2,000} F_{J''}(T) k_{\text{Abs}}} \tag{7}$$

where $F_{CO_2,XY1}$ and $F_{CO_2,XY2}$ are the fraction of CO_2 molecules in the fluorescing vibrational states that were monitored (i.e., states with $\nu_3 = 1$ or 2 here), respectively, $F_{\text{CO}_2,000}$ is the fraction of CO_2 molecules in the absorbing vibrational state, $F_{J''}$ is the Boltzmann fraction in the absorbing rotational state, and $A_{001\to000}$ and $A_{002\to001}$ are the Einstein A coefficients for the $\nu_3 = 1 \to 0$ and $\nu_3 = 2 \to 1$ emission bands, respectively. $A_{001\to000} \approx 420\ \text{s}^{-1}$ [19] and the A coefficients for emission from higher levels are approximated to scale linearly with quantum number. The values of FQY reported here are approximately 50× larger than those reported in Chapter 3 of [20] due to the lower temperatures (300 K instead of 1000 K) and mixtures (CO_2 in Ar compared with $CO_2 + H_2O$ in N_2) of interest here. In the interest of simplicity, it can be shown that the FQY for CO_2 dilute in Ar ignoring collisional excitation and assuming weak-excitation and steady state is approximately:

$$\text{FQY}_{\text{SS}} \approx \frac{A_{001\to000}}{(n_{\text{Ar}} k_{\text{VT},001\to030/110} + k_{\text{Emiss}} + A_{001\to000})} \tag{8}$$

where n_{Ar} is the number density of argon, $k_{\text{VT},001\to030/110}$ is the sum of rate constants for intermodal VT transfer to the energy levels corresponding to 030 and 110 for CO_2–Ar collisions which was modeled as equal to that of CO_2–N_2 collisions. For experiments in argon at 1 bar and 296 K, Eq. 8 is accurate to within ≈20 % of that calculated using Eq. 7 and the detailed kinetic model presented in Sect. 4.2. The reader should also note that the FQY can vary with optical power, fluence, and pumping method (CW vs. pulsed) if changing these variables alters state populations and the energy-transfer processes responsible for quenching. Therefore, caution should be taken when using these values with strategies different than reported here.

The *fraction collected* is given by Eq. (9):

$$\text{Fraction collected} = \frac{\Omega}{4\pi} \eta \tag{9}$$

where Ω (sr) is the solid angle of collection and η is the collection efficiency which is dictated by the fractional transmission of the collection optics and radiative trapping. More information regarding the influence of fluorescence trapping can be found in Sect. 7.3.

2.2 Calculation of gas properties

By scanning the laser across absorption transitions slowly compared to the characteristic time required for the fluorescing states to reach steady state (τ_{SS}) and decay back to thermal equilibrium (τ_{Decay}), the LIF signal will trace the absorption lineshape (see Sect. 6.2). As a result, gas properties can be calculated from scanned-wavelength LIF signals in a manner that is analogous to scanned-wavelength direct-absorption techniques.

Calculation of χ_i: If the FQY and collection efficiency are known and fluorescence trapping is negligible or known, the mole fraction of the absorbing/fluorescing species can be calculated from the integrated area under the LIF signal, A_{LIF}, or the LIF signal at a given wavelength by comparing measured signals to simulated signals.

Calculation of T: If the laser is scanned across two rovibrational absorption transitions within the same vibrational band such that the FQY for both transitions are equal and their lower-state energies are different, the two-color ratio of integrated areas under each LIF signal is equal to the ratio of absorption transition

linestrengths that is a function of temperature only [i.e., $A_{\mathrm{LIF},2}/A_{\mathrm{LIF},1} = S_2(T)/S_1(T) = f(T)$].

Calculation of P: The gas pressure can be calculated from the best-fit collisional width obtained from least-squares fitting a lineshape model (e.g., Voigt profile) to the LIF signal as a function of laser wavelength ($P = \Delta\nu_c/2\gamma_{\mathrm{mix}}$).

Calculation of V: The velocity of the gas can be inferred from the Doppler-shifted LIF signal that is imaged along a beam path or sheet with a component in the direction of the flow.

It should be noted that when using this approach the calculation of temperature, pressure, and velocity are independent of FQY and radiative trapping. By taking a two-color ratio of LIF signals, the dependence on FQY and radiative trapping drops out since they are identical for all rovibrational transitions within the same vibrational band (provided that the rotational states maintain a Boltzmann distribution). In addition, the pressure and velocity measurements only rely on the spectral shape or shift of the LIF signal and, therefore, do not depend on the FQY or radiative trapping provided that the SNR is large enough.

3 Species and wavelength selection

The asymmetric-stretch fundamental-vibration band of CO_2 was chosen for IR-LIF and IR-PLIF for four primary reasons. (1) It is an exceptionally strong absorption and emission band with an Einstein A coefficient of $420\,s^{-1}$, which is more than 10 times larger than of any H_2O, CO, or other CO_2 bands [18–20]. (2) It can now be accessed via relatively high-power, narrow-linewidth, wavelength-tunable lasers. (3) Highly sensitive cryogenically cooled InSb detectors and cameras are available to detect its fluorescence at 4.3 μm. (4) Spatially resolved measurements of CO_2 are relevant to a broad range of applications including combustion systems and industrial processing.

The P(36) and P(42) CO_2 transitions were used to provide a more robust sensor package that utilizes a commercially available band-pass filter to reject scattered laser light. Figure 2 shows the absorbance spectrum of CO_2 and the transmission curve of the band-pass filter used. The filter attenuates light near the linecenter of these transitions by 97–99 % to provide background-free LIF measurements of CO_2. However, if scattered laser light is not a concern, use of CO_2 absorption transitions that are 3.3–6.6 times stronger could be used for even larger LIF signals and lower detection limits if the corresponding increased degradation in laser power across the volume of interest is not problematic or can be accounted for.

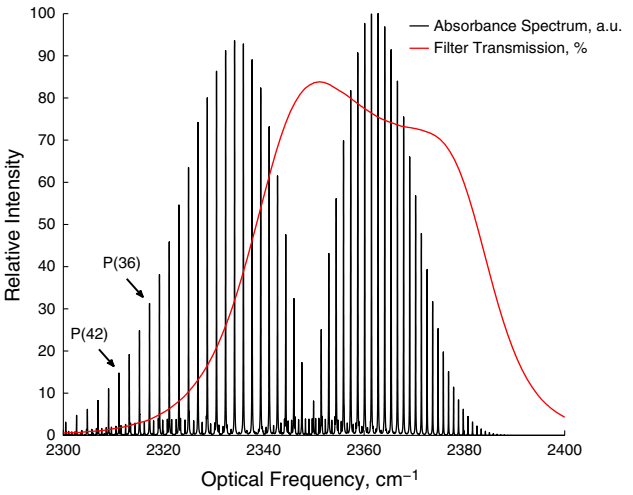

Fig. 2 Peak-normalized absorbance spectrum of CO_2 at 0.4 bar and 296 K and transmission curve for the band-pass filter used in LIF experiments

4 Spectroscopic and kinetic models for quantitative IR-LIF of CO_2

4.1 Spectroscopic database and model

The P(36) and P(42) absorption transitions near 2317.2 and 2311.1 cm^{-1}, respectively, were used to excite the ν_3 vibration band of CO_2. The P(23) transition near 2317.1 cm^{-1} was used in combination with the P(36) transition for LIF thermometry. The linestrengths of each transition were taken from the HITRAN 2012 database [19] and were found to be accurate to within 2 %, as expected [21]. A Voigt profile was used to model the lineshape of each transition, and measured collisional-broadening coefficients were used to accurately model the absorbance at linecenter as a function of pressure and composition. N_2- and Ar-broadening coefficients were measured at 0.4–1 bar using a common scanned-wavelength direct-absorption technique [22]. Table 1 presents the most relevant spectroscopic parameters.

4.2 Kinetic model and IR photophysics

Kinetic models were developed using the general methodology of Kirby [20] (with a number of modifications) who acknowledged more than 80 vibrational states and 14,000 energy-transfer processes to predict the LIF signal from the ν_3 band of CO_2 as a function of gas properties and laser parameters. While both models presented here are considerably less complex, they are hereafter referred to as "simplified" and "detailed" kinetic models. The simplified model (see Fig. 1) operates by calculating the fractional

Table 1 Spectroscopic parameters for CO_2 absorption transitions used

HITRAN 2012					Current study	
Line	ν_o	S(296 K)	E''	γ_{Air}(296 K)	γ_{N_2}(296 K)	γ_{Ar}(296 K)
	cm^{-1}	$cm^{-2}atm^{-1}$	cm^{-1}	$cm^{-1}atm^{-1}$	$cm^{-1}atm^{-1}$	$cm^{-1}atm^{-1}$
P(42)	2311.1	11.78	704.3	0.079	0.068	0.051
P(23)[a]	2317.1	2.67	882.9	0.097	–	–
P(36)	2317.2	24.80	519.5	0.085	–	0.051

Uncertainty of measured collisional-broadening coefficients is <5 %

[a] Indicates transition from $\nu_1\nu_2\nu_3$ of 010 to 011, all other transitions are for 000 to 001

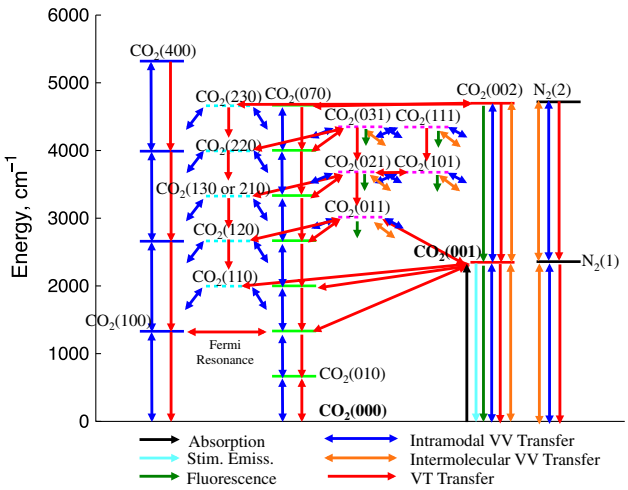

Fig. 3 Detailed energy-level diagram for IR-LIF of CO_2 at 4.3 µm. All states and energy-transfer processes used in the detailed kinetic model are shown here

population of CO_2 molecules in seven vibrational levels according to the most significant radiative and collision-induced energy-transfer processes, whereas the detailed model (see Fig. 3) acknowledges 23 different vibrational levels for improved accuracy. All rotational states are assumed to be unperturbed by laser pumping and, therefore, maintain a Boltzmann population according to the gas temperature. This assumption is accurate given that the rate constant for rotational-energy transfer (RET), given by Eq. 10, is 2–3 orders of magnitude faster than the fastest vibrational-energy-transfer (VET) processes and 6–7 orders of magnitude faster than the fastest radiative processes.

$$k_{RET} = 2\pi c \Delta\nu_c \tag{10}$$

For simplicity, vibrational modes are assumed to be independent and harmonic and the energy-transfer rates are treated as independent of the axial spin momentum of the vibrational levels. As a result, simplified notation is used to define the vibrational states of CO_2 using only three quantum numbers: ν_1, ν_2, and ν_3; for example, a state labeled "120" indicates that $\nu_1 = 1, \nu_2 = 2, \nu_3 = 0$. The rate constants used in this work have been scaled appropriately to be consistent with this approach given the degeneracy of each vibrational mode; more information validating this simplified approach can be found in Appendix C of [20].

4.2.1 *Radiative transfer*

Both kinetic models account for energy transfer due to laser absorption, stimulated emission, and fluorescence. Laser absorption transfers CO_2 molecules from the absorbing vibrational and rotational states to an excited ν_3 state (e.g., 001) and upper rotational state. Collisions quickly equilibrate the rotational states of the vibrationally hot molecules to a Boltzmann distribution and stimulated emission transfers CO_2 molecules in the upper vibrational and rotational states back down to the absorbing state. Unlike stimulated emission, fluorescence can occur for CO_2 molecules in any rotational state (that is IR active) in an excited ν_3 state such that the fluorescence spectrum mirrors that of absorbance. The rate coefficients of absorption and stimulated emission are given by Eqs. (3) and (6). It should be noted that the ν_2 vibrational mode also fluoresces, but it is not of interest here and does not significantly alter the fractional population within the ν_2 mode.

4.2.2 *Collision-induced vibrational-energy transfer*

Collisions can shuffle CO_2 into different vibrational states via four primary mechanisms: (1) Intramodal vibration-translation (VT) transfer occurs when a collision moves CO_2 up or down in vibrational energy with the energy difference going to (or coming from) translational energy of the collision partner. Due to the large vibrational-energy-level spacing, these processes are relatively slow at low temperatures, but any excess energy transferred to the collision partner is quickly equilibrated within the molecular ensemble. (2) Intermodal VT transfer occurs when a collision shuffles CO_2 into a different vibrational state (usually of comparable energy) with the energy difference being

transferred to (or from) translational energy of the collision partner. These processes can be fast, even at low temperatures, if the energy difference between the initial and final state is small. One important example of intermodal VT transfer for this work is $CO_2(001) + M \leftrightarrow CO_2(110) + M$. (3) Intramodal vibration-vibration (VV) transfer occurs when two CO_2 molecules collide and exchange vibrational energy to move toward or maintain a Boltzmann distribution within that vibrational mode; these processes are extremely fast due to them being near resonant. (4) Intermolecular VV transfer can occur when CO_2 collides with a different molecule with a similar vibrational-energy-level spacing (e.g., N_2 or CO). These processes are also extremely fast when they are near resonant. One important example of intermolecular VV transfer is that between the ν_3 mode of CO_2 and N_2 [e.g., $CO_2(001) + N_2(0) \leftrightarrow CO_2(000) + N_2(1)$]. Table 2 presents some example rates for a condition of interest here, and Table 3 presents some of the most pertinent rate constants for VET used in the kinetic models. Unless noted otherwise, the rate constants listed in Table 3 were taken from Appendix C of [20] which provides the original sources. The rate constant for VT equilibration of the ν_2 mode in Ar listed in [23] was used here since it enabled more accurate LIF simulations than that used in [20].

Table 2 Example rates for various energy-transfer processes for pumping the P(42) CO_2 line at 1 bar, 296 K, and with 1 % CO_2 in N_2 and a 100-mW, 2-mm-diameter laser beam at the absorption transition linecenter

Rates (s^{-1})	
$A_{001\rightarrow000}$	$= 4.20 \times 10^2$
$nk_{VT,001\rightarrow000}$	$= 5.90 \times 10^2$
k_{Abs}	$= 1.20 \times 10^3$
$nk_{VT,001\rightarrow110}$	$= 1.04 \times 10^5$
$n_{N_2}k_{VV,001\rightarrow000}$	$= 2.77 \times 10^7$
$n_{CO_2}k_{VV,001\rightarrow000}$	$= 2.99 \times 10^7$
k_{RET}	$= 2.56 \times 10^{10}$

4.2.3 Additional approximations

A harmonic oscillator approximation was used to scale higher-order rate constants linearly with vibrational quantum number with the exception of the VV equilibration of the ν_2 mode that was modeled as described in [24]; for example, the reaction $CO_2(002) + CO_2(000) \rightarrow CO_2(001) + CO_2(001)$ proceeds twice as fast as the reaction $CO_2(001) + CO_2(000) \rightarrow CO_2(000) + CO_2(001)$. Furthermore, rate constants for transfer within a given vibrational mode are modeled as independent of the vibrational energy within the other modes; for example, $CO_2(001) + CO_2(000) \rightarrow CO_2(000) + CO_2(001)$ proceeds at the same rate as $CO_2(001) + CO_2(XY0) \rightarrow CO_2(000) + CO_2(XY1)$ for all X and Y. In addition, several intermodal VT-transfer rate constants needed in the detailed model are not known and, therefore, were estimated by comparison with similar processes; for example, the intermodal VT transfer out of 011, 021 and 101, and 031 and 111 were modeled as 8, 12, and 16 times faster than $k_{VT,001\rightarrow110}$, respectively, for $M = N_2$, and 3.4, 5.1, and 6.8 times faster for M=Ar, respectively. These scaling factors were chosen to provide the best agreement between simulated and measured LIF signals shown in Figs. 6 and 7, but do not significantly influence the simulated LIF signals at pressures >0.25 bar.

4.2.4 Rate equations

With the dominant rate constants known, first-order differential equations were evaluated numerically to calculate the fraction of CO_2 molecules in each vibrational state in the

Table 3 Rate constants for the most significant VET processes

Reaction #	Reaction	Rate constants, at 296 K, $cm^3 molecule^{-1} s^{-1}$
1	$CO_2(001) + M \rightarrow CO_2(000) + M$	$= 2.37 \times 10^{-17}$
2	$CO_2(001) + M \rightarrow CO_2(011) + M$	$= 8.06 \times 10^{-17}$
3	$CO_2(010) + M \rightarrow CO_2(000) + M$	$= 3.24 \times 10^{-15}$
4	$CO_2(001) + M \rightarrow CO_2(110) + M$	$= 4.17 \times 10^{-15}$
5	$CO_2(001) + M \rightarrow CO_2(030) + M$	$= 4.17 \times 10^{-15}$
6	$CO_2(000) + N_2(1) \rightarrow CO_2(001) + N_2(0)$	$= 1.12 \times 10^{-12}$
7	$CO_2(100) + M \rightarrow CO_2(020) + M$	$= 3.84 \times 10^{-12}$
8	$CO_2(010) + CO_2(000) \rightarrow CO_2(000) + CO_2(010)$	$= 5.70 \times 10^{-11}$
9	$CO_2(100) + CO_2(000) \rightarrow CO_2(000) + CO_2(100)$	$= 1.20 \times 10^{-10}$
10	$CO_2(001) + CO_2(000) \rightarrow CO_2(000) + CO_2(001)$	$= 1.20 \times 10^{-10}$

Rate constants for the reverse direction are given by $k \times \exp(-E/k_bT)$ where E is the energy difference between the two states (e.g., $E = 667\,cm^{-1}$ for reaction #3)

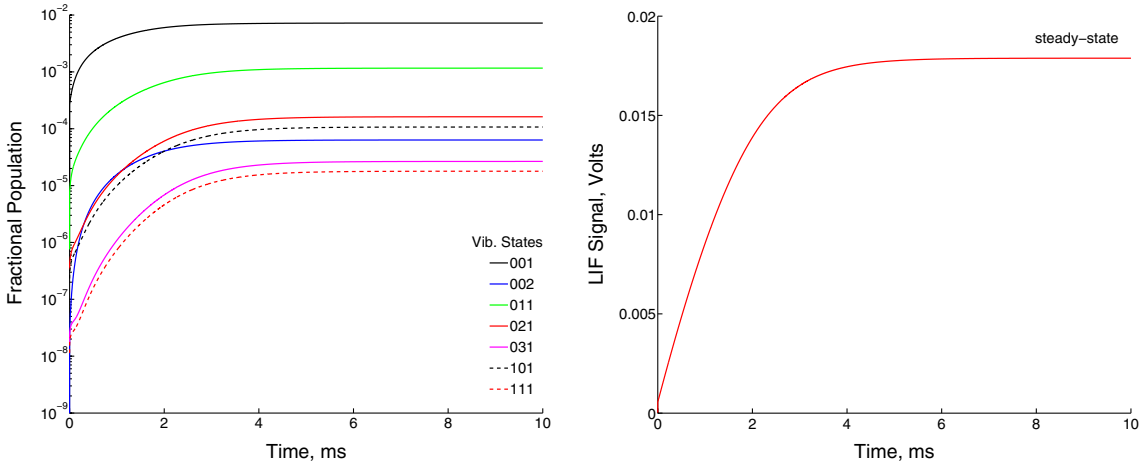

Fig. 4 Simulated fractional population in fluorescing CO_2 vibrational states (*left*) and corresponding simulated LIF signal (*right*) using the detailed kinetic model with $P = 0.13$ bar, $\chi_{CO_2} = 0.43$ % in N_2 with a 100-mW, 2-mm-diameter laser beam pumping the P(42) transition at linecenter

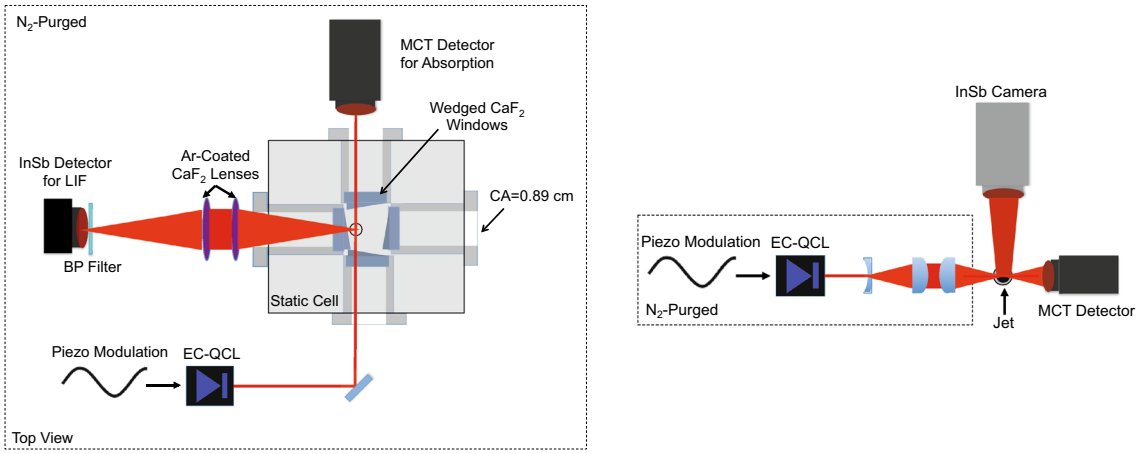

Fig. 5 Experimental setup used in IR-LIF experiments (*left*) and IR-PLIF experiments (*right*)

presence of laser radiation. At $t = 0$, all populations are set equal to that corresponding to thermal equilibrium at the gas temperature. Laser pumping is initiated at $t = \Delta t$. Eq. (11) provides an abbreviated equation describing the number density of CO_2 molecules in the 001 state; however, only Eqs. (12) and (13) are actually evaluated (for every state) in the model to avoid numerical precision errors. Analogous equations are solved for N_2 vibrational states when applicable.

$$\begin{aligned}\frac{\mathrm{d}n_{CO_2,001}(t)}{\mathrm{d}t} &= n_{CO_2,000}(t-\Delta t)F_{J''}(T)k_{Abs} \\ &- n_{CO_2,001}(t-\Delta t)F_{J'}(T)k_{Emiss} \\ &- n_{CO_2,001}(t-\Delta t)A_{001\to000} \\ &- n_{CO_2,001}(t-\Delta t)n_M k_{\mathrm{VT},001\to110} \\ &+ n_{CO_2,110}(t-\Delta t)n_M k_{\mathrm{VT},110\to001} + \cdots \end{aligned} \tag{11}$$

$$\frac{\mathrm{d}F_{CO_2,001}(t)}{\mathrm{d}t} = \frac{1}{n_{CO_2}}\frac{\mathrm{d}n_{CO_2,001}(t-\Delta t)}{\mathrm{d}t} \tag{12}$$

$$F_{CO_2,001}(t) = F_{CO_2,001}(t-\Delta t) + \frac{\mathrm{d}F_{CO_2,001}(t-\Delta t)}{\mathrm{d}t}\Delta t \tag{13}$$

Here, n_{CO_2} is the total number density of CO_2 (molecules cm^{-3}), n_M is the number density of any collision partner, M, for which the rate constant applies, Δt is the time step of the simulation (5–10 ns here), and $F_{J''}$ and $F_{J'}$ are the fraction of CO_2 molecules in the lower and upper rotational states, respectively, which are a function of temperature only.

Figure 4 (left) shows the fractional population in the fluorescing CO_2 vibrational states for a simulation conducted using the detailed model at 0.13 bar with 0.43 % CO_2 in N_2 and 100 mW of laser power. At this pressure,

the population in each excited state rises to its steady-state value in ≈4 ms. With the populations in the vibrational states known, simulated LIF signal can be calculated using the relations presented in Sect. 2. Figure 4 (right) shows the corresponding simulated LIF signal for this condition with the collection and detection parameters given in Sect. 5.

5 Experimental setups for LIF and PLIF measurements

5.1 LIF setup

A simplified schematic of the experimental setup used for IR-LIF is shown in Fig. 5 (left). Absorption and LIF measurements were acquired simultaneously with ≈0.5 % CO_2 in Ar or N_2 at 0.007 to 1 bar in a static cell. The cell has a 1.4 cm path length and 4 CaF_2 windows each with a 3-deg wedge. An external-cavity quantum-cascade laser (Daylight Solutions) producing 100–120 mW and a linewidth <5 MHz near 4.3 μm was used to excite transitions in the asymmetric-stretch fundamental-vibration band of CO_2. The amount of laser power entering the static cell was measured using a broadband power meter (Ophir) and the Gaussian waist of the laser beam was 1.9 mm. During scanned-wavelength experiments, the laser's wavelength was tuned across a rovibrational transition by sinusoidally modulating the piezo motor at 10–100 Hz. Prior to all experiments, the static cell was evacuated to <0.013 mbar and the light intensity transmitted through the static cell was measured and later used to calculate the absorbance of the test gas in subsequent tests. A solid germanium etalon with a free spectral range of 0.0163 cm^{-1} was used to characterize the wavelength tuning of the laser. More information regarding the use of this laser can be found in [21]. A thermoelectrically cooled mercury-cadmium-telluride (MCT) detector (Vigo Systems) with a 10-MHz bandwidth was used to measure the laser light transmitted through the static cell.

LIF was imaged orthogonal to the laser beam using an anti-reflection-coated CaF_2 doublet (25.4 mm diameter and focal length) providing a solid angle of collection of 0.1 sr and a liquid-N_2-cooled InSb detector (IR associates) with a 2-mm-diameter active area (providing a spatial resolution of 2 mm with the doublet used here) and an external amplifier of variable gain. The detector and amplifier produced 3.27×10^5 V/W at 4.3 μm with a gain of 1x according to the manufacturer's specifications, and this was verified within experimental uncertainty of 12 %. A band-pass filter (Spectrogon NB-4245-090 nm) was used to reject scattered laser light and pass 54.7 % of the fluorescence from the $\nu_3 = 1 \rightarrow 0$ band of CO_2 (according to the manufacturer's transmission curve and simulations performed using the HITRAN 2012 database). After accounting for reflection losses, the total collection efficiency (η) of the optical setup was 0.49. Fluorescence trapping losses inside the gas cell reduced the collected LIF signal by an additional 2–8 % and was accounted for in the analysis. The entire optical setup was purged with N_2 to minimize laser absorption and fluorescence trapping outside the gas cell. All signals were acquired at a sampling rate of 200 kHz–1 MHz with DC coupling using a National Instruments data acquisition system (PXI-6115).

5.2 PLIF setup

A simplified schematic of the experimental setup used for IR-PLIF is shown in Fig. 5 (right). In scanned-wavelength experiments, the wavelength of the laser was tuned ≈0.5 cm^{-1} across the P(42) transition of CO_2 near 2311.1 cm^{-1}. Ar-coated BaF_2 plano-concave and plano-convex lenses with a focal length of –40 and 200 mm, respectively, were used to expand the 1.9 mm laser beam to a full width at half maximum (FWHM) of 5 mm. A CaF_2 cylindrical lens with a focal length of 18 cm was used to focus the expanded laser beam into a sheet with a thickness (FWHM) of 500 μm. Of the original 120 mW of laser power, only 80 mW reached the field of view due to reflections, and most significantly, absorption by ≈100 ppm of CO_2 along the beam path.

An InSb camera (Telops FAST 650) was used to image the IR-PLIF of CO_2 near 4.3 μm without an optical filter (scattered laser light was not observed in the images). The camera's full window (640 × 512 pixels) was used in all images with a frame rate of 330 frames per second (FPS) and an exposure time of 100 μs. The projected pixel size of all presented images is ≈40 μm and was calculated from images of static emitters of known size. Prior to each experiment, 100 dark images were recorded, averaged, and subtracted from each individual flow-field image. A MCT detector (Vigo Systems) was used to simultaneously monitor the path-integrated laser absorption through the jet.

Images were acquired in laminar and unsteady jets of 0.5 % CO_2 in Ar with and without Ar co-flow. The inner diameter of the core jet is 4.1 mm, and the co-flow jet has a diameter of 25.4 mm. Prior to entering the jet, independent streams of CO_2 and Ar were regulated with flow meters and combined in a mixing manifold to achieve the desired mole fraction of CO_2.

6 LIF results

6.1 Fixed-wavelength IR-LIF for kinetic model evaluation

Experiments were first conducted with the laser wavelength fixed on the absorption transition linecenter to evaluate the steady-state performance of the kinetic models used to simulate LIF signals. Figure 6 shows the measured steady-state LIF signal with a detector gain of 1× (left) and the corresponding measured FQY (right) as functions of total gas pressure. With ≈120 mW of laser power, the LIF signal increases with increasing pressure until collisional broadening and quenching take over near 0.1 bar. The measured FQY in argon decreases monotonically with increasing pressure and the simulated FQY agrees well with measured values, especially at pressures above 0.4 bar. Figure 7 shows the measured and simulated LIF signals (left) and FQY (right) for experiments conducted in N_2. Again the LIF signal increases with increasing pressure until collisional broadening and quenching take over, near 0.13 bar in N_2. However, the FQY in N_2 exhibits more complex behavior than for Ar. First, the FQY decreases with increasing pressure up to ≈0.02 bar, then increases with increasing pressure up to 0.13 bar, and lastly decreases with increasing pressure beyond 0.13 bar. The FQY simulated with the detailed model captures these trends, but with some error in magnitude and location of inflection points. The measured and simulated LIF signals (using the detailed model) also agree well with each other, especially at pressure above 0.4 bar.

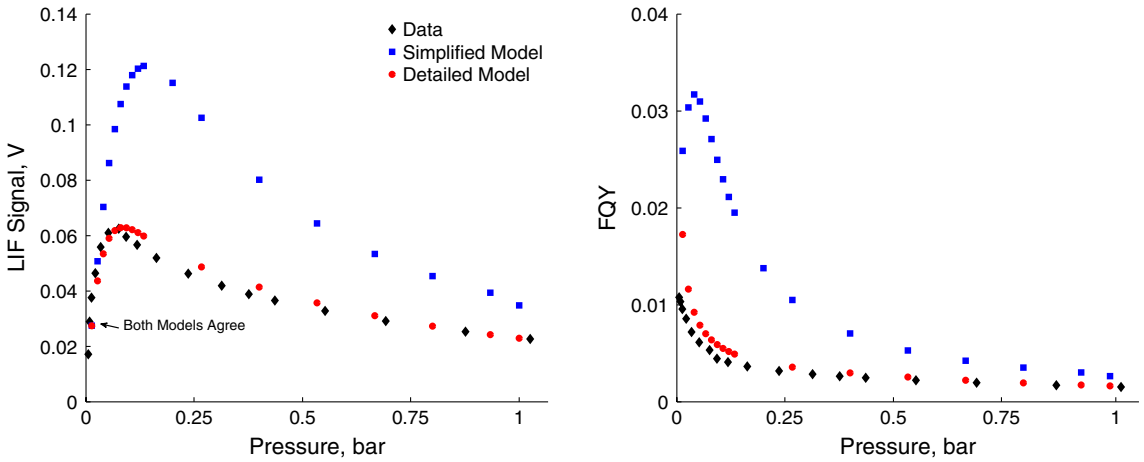

Fig. 6 Measured and simulated LIF signals (*left*) and FQY (*right*) for fixed-wavelength experiments conducted in Ar with $\chi_{CO_2} = 0.0054$ and 120 mW of laser power pumping the P(36) transition at linecenter. *Error bars* are too small to be seen

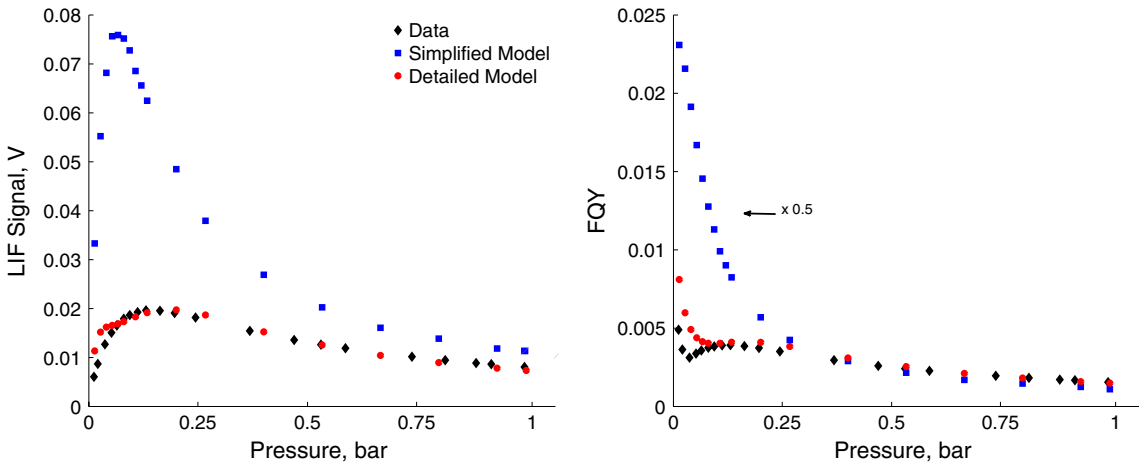

Fig. 7 Measured and simulated LIF signals (*left*) and FQY (*right*) for fixed-wavelength experiments conducted in N_2 with $\chi_{CO_2} = 0.0043$ and 100 mW of laser power pumping the P(42) transition at linecenter. *Error bars* are too small to be seen

It is important to note that all quantities presented in Figs. 6 and 7 depend on the laser power, gas composition, and temperature. Increased laser power pushes the maximum LIF signal to greater pressures and increases the LIF signal. For $\chi_{CO_2} < 0.01$ in Ar or N_2 the FQY is nearly independent of χ_{CO_2}, varying by only 0.2 %.

Comparing the results from the simplified and detailed kinetic models provides insight to the dominant processes that dictate the LIF signal. In general, the LIF signal calculated using the simplified model overpredicts that of the detailed model. This is because the simplified model constrains all of the CO_2 molecules to a smaller number of states, thereby leading to greater population in the fluorescing states and, therefore, greater LIF signal. In reality, the excess vibrational energy acquired from laser absorption flows to all vibrational states via collisions, thereby, reducing the population in the fluorescing states. As a result, in order for the simplified and detailed models to produce the same LIF signal, collisions must be (1) so rare or ineffective that they do not alter the population in the fluorescing states or (2) so pronounced that they prevent any one vibrational state from being significantly excited. These two conditions are hereafter referred to as the low-pressure and high-pressure limits. Figures 6 and 7 indicate that the low-pressure limit occurs around 25 mbar for CO_2 in Ar, but at much lower pressures in N_2 due to fast intermolecular VV transfer. Conversely, the high-pressure limit was nearly reached in N_2 (occurs near 2.6 bar in N_2), but not in Ar where the comparatively slow VT transfer is the primary mechanism for deactivating the CO_2 ν_3 band.

In all cases, the disagreements between measured and simulated LIF signals and FQY at lower pressures are most likely a result of acknowledging too few vibrational states in the kinetic models. At low pressures, many excited vibrational levels are significantly populated, and therefore, energy transfer between more states (than addressed here) must be acknowledged to accurately model the population within any given level. That said, more rate constants must also be known to accurately model the populations in the many excited states that exist at low pressures. Regardless, the exceptional agreement between measured and simulated quantities (using the detailed model) above 0.4 bar suggests that the detailed model and most significant rate constants presented in Sect. 4.2.2 are accurate.

6.2 Scanned-wavelength IR-LIF

Scanned-wavelength experiments are presented to demonstrate the ability of this technique to infer absorption spectra from LIF data and, therefore, provide spatially resolved measurements of temperature, pressure, composition, and velocity analogous to scanned-wavelength direct-absorption techniques [3].

6.2.1 *IR-LIF measurements of temperature, pressure and* χ_{CO_2}

Figure 8 shows the measured absorbance and LIF signals while sinusoidally modulating the wavelength of the EC-QCL at 10 Hz (left) and peak-normalized signals with the best-fit Voigt profile (right). The LIF signal is corrected for the laser intensity modulation and wavelength-dependent absorption along the line of sight that occurs prior to the volume of gas being imaged. The LIF signal traces the absorbance profile and the best-fit Voigt profile applied to the LIF signal recovers the known collisional width and, therefore, gas pressure within 2 % of the known value. The best-fit integrated area (2.9×10^{-3} V per cm^{-1}) agrees

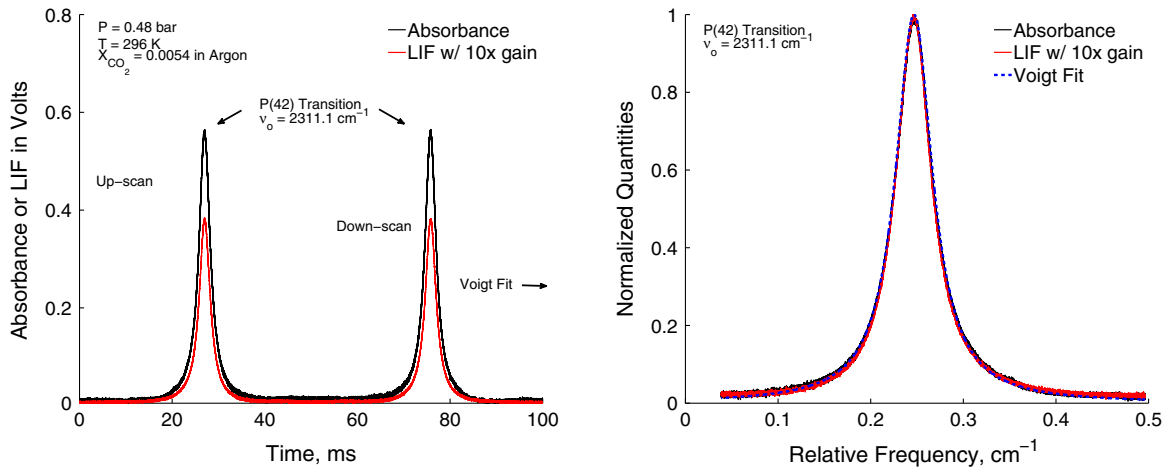

Fig. 8 Measured absorbance and LIF signal during 1 complete modulation period (*left*) and peak-normalized absorbance, LIF signal, and best-fit Voigt profile for a single spectrum (*right*)

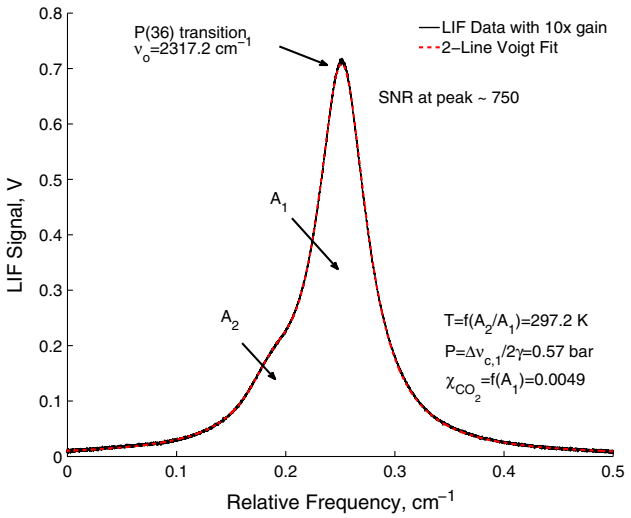

Fig. 9 Measured LIF signal and best-fit Voigt profiles for a single scan across two CO_2 absorption transitions $\chi_{CO_2} = 0.005$. The best-fit collisional width and integrated areas of the two transitions enable measurements of temperature, pressure, and χ_{CO_2} within 2 % of known values

within 6 % of that calculated using the detailed kinetic model and, therefore, recovers the known χ_{CO_2} within 6 %. Measurements of χ_{CO_2} and pressure were repeated at pressures up to 1 bar in argon and recovered known values within 1–8 % where the accuracy steadily improved with increasing pressure.

Figure 9 shows the measured LIF signal and best-fit Voigt profiles for a single scan at 20 Hz across two CO_2 absorption transitions in the ν_3 band. The temperature, pressure, and χ_{CO_2} calculated using the best-fit integrated areas and collisional width (of the P(36) transition) agree within 2 % of known values. It should be noted that when using two transitions in different excited vibrational states (011 and 001 here), the pressure must be sufficient to equilibrate the fluorescing ν_3 states (>0.4 bar here) in order for the FQY to be equal for both transitions. This requirement can be avoided by using two different rovibrational transitions with the same upper vibrational state as is recommended in Sect. 2.2. Furthermore, isolated transitions with a larger difference in lower-state energy should be used for a more sensitive and robust IR-LIF thermometer.

6.2.2 *Influence of scan rate and τ*

If the laser is scanned across the absorption transition fast compared with τ_{SS} or τ_{Decay}, then the LIF signal will not trace the absorbance spectrum (see Fig. 10). Figure 10 (left) shows measured absorbance and LIF signals in Ar at 66 mbar for two consecutive scans. The LIF signal exhibits an abrupt rise when the laser becomes resonant with the absorption transition and then decays once the laser moves off the absorption transition. In Ar the energy transfer is relatively fast and the results shown in Fig. 10 indicate that $\tau_{Decay} \approx 0.33$ ms even at only 66 mbar. However, in N_2 τ_{SS} and τ_{Decay} are much longer since the vibrational mode of N_2 can store and release a large amount of energy (from and to CO_2) analogous to a large capacitor when VT relaxation of N_2 is slow (e.g., at low temperatures and/or in absence of H_2O as is the case here). Figure 10 (right) shows that at 0.124 bar, $\tau_{Decay} \approx 12$ ms, and thus, ≈36 ms must pass before the LIF signal has decayed to 5 % of its peak signal. To further demonstrate the accuracy of the detailed kinetic model, Fig. 10 also shows the simulated LIF signal as function of time calculated with a time-varying absorbance.

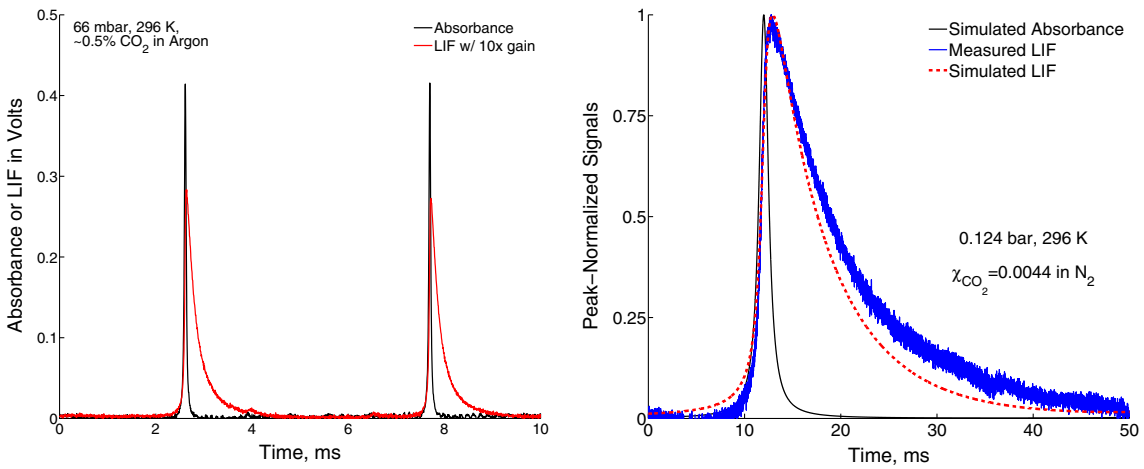

Fig. 10 Measured absorbance and LIF signal in Ar (*left*) and N_2 (*right*) with fast wavelength scanning (compared to τ_{SS} and τ_{Decay}). Simulated LIF signal (*right*) was calculated using the detailed kinetic model

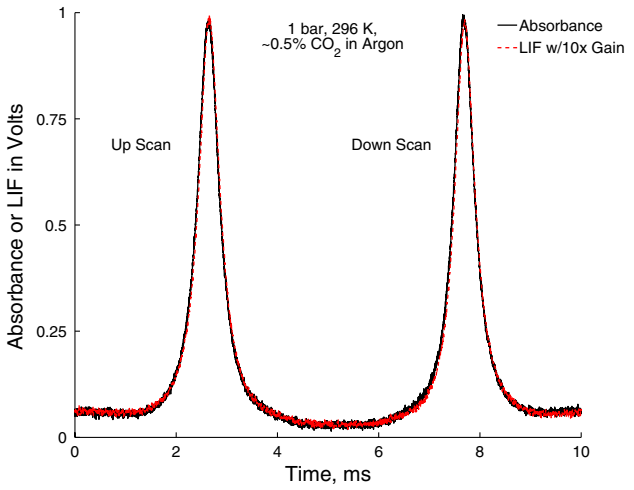

Fig. 11 Peak-normalized absorbance and LIF signals measured at 200 Hz in Ar with $\chi_{CO_2} = 0.0054$ at 1 bar

While differences do exist, the simulated signal tracks the measured LIF signal well indicating that the dominant rate constants and states are modeled accurately in the detailed kinetic model presented in Sect. 4.2.2. Conversely, if the quenching rates and FQY cannot be calculated a priori (e.g., due to unknown gas composition or temperature), fast wavelength scanning could be employed to measure the local decay (i.e., quenching) rate out of the fluorescing state for calibration of the kinetic models presented in Sect. 4.2.

Increasing the gas pressure decreases τ_{Decay} (via increased collision frequency) and, therefore, enables faster measurements of absorbance spectra via LIF. Figure 11 shows peak-normalized absorbance and LIF signals for one complete modulation period with the laser scanning across the P(42) transition at 200 Hz. The LIF signal traces the absorption spectrum enabling measurements of pressure and χ_{CO_2} at 200 Hz via scanned-wavelength LIF. It should be noted that some distortion in LIF signals was observed at faster scan rates, indicating that 200 Hz is close to the maximum repetition rate possible at 1 bar with 0.5 % CO_2 in Ar at 296 K. Increasing the gas pressure, temperature, or χ_{CO_2} could enable faster measurement rates, but likely at the cost of reduced LIF signals via increased quenching.

7 PLIF results

7.1 Fixed-wavelength PLIF

Fixed-wavelength experiments with the laser centered on the P(42) transition's linecenter were conducted to image unsteady CO_2–Ar jets. Figure 12 (top) shows three consecutive images of a free jet with a Reynolds number, $Re_D = \rho UD/\mu$, of 2760 where ρ, U, and μ are the gas density, velocity, and viscosity, respectively, and D is the inner diameter of the core jet. The images highlight the unsteady structure of the jet, which is consistent with its Re_D, and the utility of this technique to image flow structure. A hexagonal cylinder was then placed in the center of the jet to cause the flow to bifurcate and create further structure. Figure 12 (bottom) shows three consecutive images of an obstructed jet with $Re_D = 1960$. The images indicate that each arm of the jet exhibits different degrees of unsteadiness. Several 10×10 pixel regions in the core of the free jet were used to calculate the spatial SNR (given by the mean signal divided by its standard deviation). The spatial SNR varied from 22–25 for the images with approximately 0.5 % CO_2 in Ar, 80 mW of laser power, and a 100 µs exposure time.

All images shown were corrected for the degradation of laser power across the jet (due to absorption) as follows. (1) The raw LIF signal across a row of pixels, $S_F(x)$, was converted to an approximate line-of-sight (LOS) distribution of CO_2 mole fraction, $\chi_{CO_2}(x)$, by scaling the peak-normalized (for a given row) $S_F(x)$ by the known value of χ_{CO_2} in the jet core. (2) The fraction of optical power (or irradiance) reaching a given point, x_i, was then calculated using Beer's Law: $I(x_i)/I_o = \exp[-\int_0^{x_i} S(T)P\chi_{CO_2}(x)\phi(\nu)\mathrm{d}x]$. (3) The corrected LIF signal at x_i was then calculated by multiplying the raw LIF signal at x_i by $I_o/I(x_i)$. Steps 1–3 were repeated, with $\chi_{CO_2}(x)$ now calculated in Step 1 using the corrected LIF signal, until $\chi_{CO_2}(x)$ went unchanged with subsequent iterations; typically only two iterations were needed here. The near-Gaussian power distribution of the laser sheet (in the y-direction) was not corrected for.

7.2 Scanned-wavelength PLIF

Scanned-wavelength experiments were conducted in a laminar CO_2–Ar jet with $Re_D = 690$ in Ar co-flow. The QCL was scanned across the P(42) transition and the PLIF signal was imaged at 330 fps. Figure 13 (*top*) shows the PLIF image of the jet at an instant in time with the laser near the transition linecenter, and Fig. 13 (*bottom*) shows the average PLIF signal in a 2×2 pixel window as a function of time. The PLIF signal traces the corresponding absorption lineshape and a best-fit Voigt profile (applied to the PLIF signal as a function of laser wavelength) yields a collisional width of 0.049 $\text{cm}^{-1}\,\text{atm}^{-1}$, which corresponds to a pressure of 0.98 bar (i.e., 3 % error).

Figure 14 shows the imaged mole fraction of CO_2 across the jet in a 5-row-average plane located 7.9 ± 0.1 mm downstream of the jet exit. The measured line-of-sight absorption was used to calibrate the imaged distribution to absolute χ_{CO_2}. In the absence of non-uniform trapping, highly precise quantitative measurements

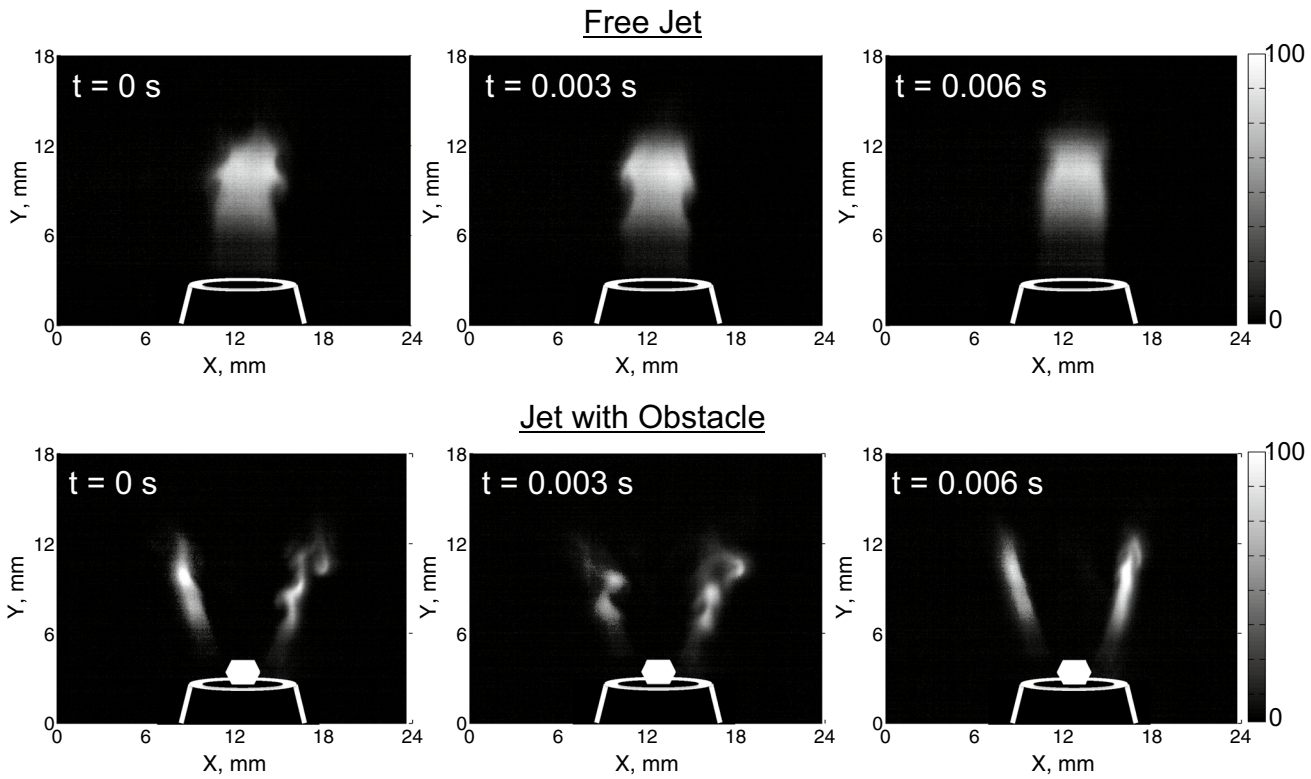

Fig. 12 Three consecutive CW IR-PLIF images of a free jet with $\mathrm{Re}_D = 2760$ (*top*) and jet with obstacle with $\mathrm{Re}_D = 1960$ (*bottom*) at 330 FPS with ≈ 80 mW of laser power pumping the P(42) CO_2 transition at linecenter

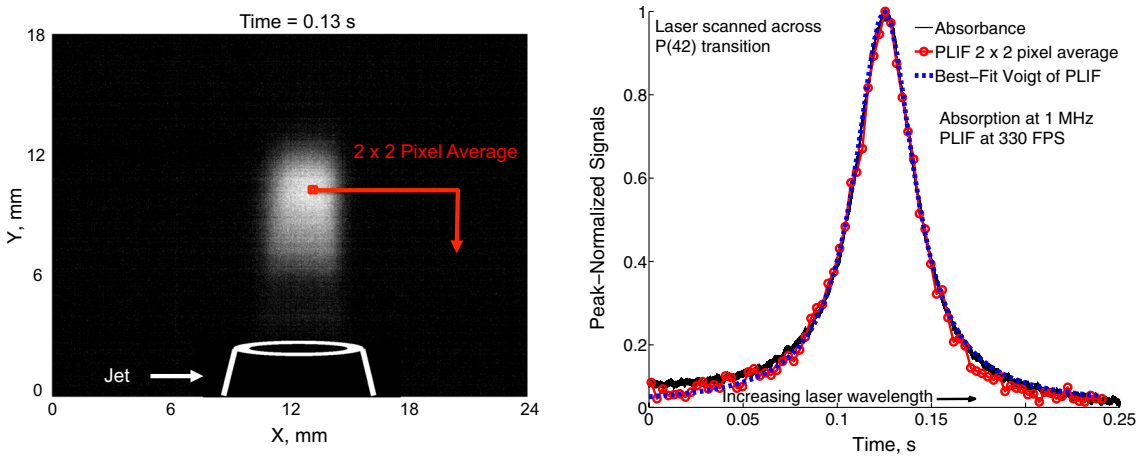

Fig. 13 Scanned-wavelength PLIF signal with the laser near the absorption transition linecenter in a laminar jet with $\mathrm{Re}_D = 690$ (*top*) and corresponding time-resolved PLIF signal (*bottom*) in a 2×2 pixel region during a scanned-wavelength experiment. The PLIF signal traces the corresponding absorption lineshape and the best-fit Voigt profile enables spatially resolved pressure measurements

of relative concentration in CO_2–Ar jets in Ar co-flow are enabled due to the absorption lineshape and FQY (i.e., quenching) being nearly independent of CO_2 mole fraction for the range of interest here; for example, the FQY and $\phi(\nu_o)$ vary by 0.15 and 0.3 %, respectively, for χ_{CO_2} between 0 and 1 % in Ar according to the model presented in Sect. 4.2. For CO_2–Ar jets ejecting into only N_2, the maximum uncertainty in FQY and $\phi(\nu_o)$ would be 15 and 25 %, respectively, due to differences in N_2-broadening and collisional quenching.

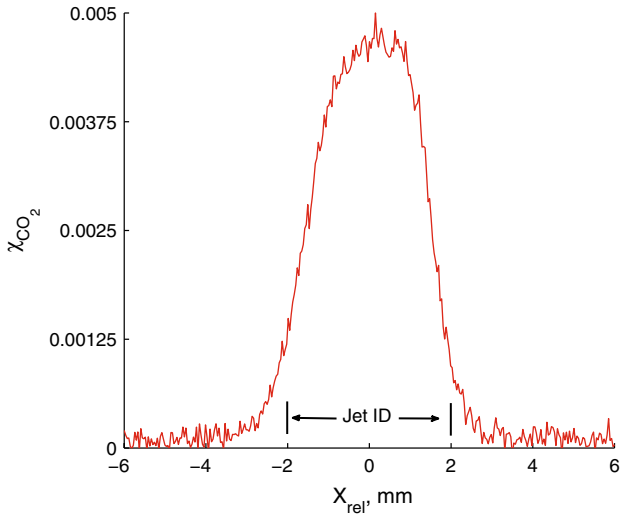

Fig. 14 Imaged distribution of χ_{CO_2} (averaged over five rows) across a laminar CO_2–Ar jet in Ar co-flow (see Fig. 13). Measurement plane is located 7.8–8.0 mm downstream of the jet exit. $X_{rel} = 0$ corresponds to the center of the jet

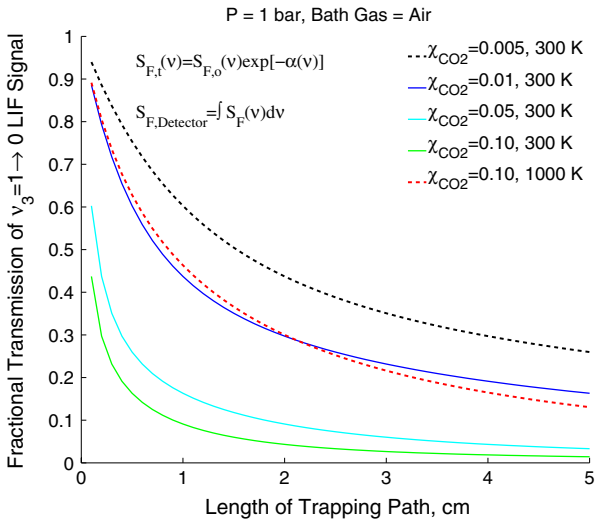

Fig. 15 Fractional transmission of $\nu_3 = 1 \rightarrow 0$ LIF signal as a function of trapping path length for various values of χ_{CO_2} at 296 K or 1000 K and 1 bar. Values were calculated using the HITRAN 2012 database assuming the emitting rotational states are in equilibrium such that the LIF signal is resonant with the absorbance spectrum of CO_2

7.3 Influence of fluorescence trapping

In IR-LIF, the fluorescence spectrum is resonant (or near resonant) with the absorbance spectrum of the absorbing/fluorescing species. As a result, the fluorescence signal is absorbed in route to the camera/detector according to Beer's Law and the gas conditions along the imaging path. For the results presented here, a reasonable estimate for the fluorescence-trapping-induced uncertainty in the imaged distribution of χ_{CO_2} is 11 % of the local value. This uncertainty corresponds to the percent decrease in LIF signal (which is assumed to be completely resonant with the absorbance spectrum) across the radius of the jet with a constant 0.5 % CO_2. Some rays (originating from points located near the perimeter of the jet) traverse a shorter distance and will be attenuated less, and other rays may traverse a slightly longer distance and be attenuated more.

Figure 15 illustrates the quasi-exponential dependence of the transmitted $\nu_3 = 1 \rightarrow 0$ LIF signal on the path length of the trapping volume and the strong dependence on χ_{CO_2} and temperature, the latter of which results primarily from partition-function effects. The dependence on the trapping path length and χ_{CO_2} can be used to assess the scalability of our technique (and CO_2 ν_3 PLIF of others [13, 15, 17]) since the FQY and line broadening exhibit a comparatively weak dependence on χ_{CO_2} [20]. In the event that larger systems or larger amounts of χ_{CO_2} are of interest, weaker absorption transitions in the ν_3 band can be pumped (if the degradation of laser power due to absorption is problematic) and the increase in fluorescence trapping losses may be tolerable due to the quasi-exponential dependence on trapping path length and χ_{CO_2}.

7.4 Comparison with past work

To provide greater insight and intuition regarding this CW IR-PLIF technique, this section will briefly compare the results reported here with those of Kirby and Hanson [13, 20] who used high-power pulsed excitation of CO_2 at 2 μm to image PLIF of CO_2 from the ν_3 band. Assuming equal gas conditions, FQY, fluorescence trapping losses, and collection efficiency (including camera response), the ratio of fluorescence signals between the current study (CS) and that of Kirby and Hanson (KH) is:

$$\frac{S_{F,\mathrm{CS}}}{S_{F,\mathrm{KH}}} \approx \frac{[\text{Photons in per } \tau_{\mathrm{Int}} \text{ per } V_{\mathrm{sheet}} \times S(T)]_{\mathrm{CS}}}{[\text{Photons in per pulse per } V_{\mathrm{sheet}} \times S(T)]_{\mathrm{KH}}} \quad (14)$$

where τ_{Int} is the integration time of the camera and V_{sheet} is the volume of the laser sheet. For the 5× larger integration times used here and assuming a 20 mJ, 6 ns pulse with 1000× less absorbance and an 8× larger laser sheet for Kirby and Hanson [13], $\frac{S_{F,\mathrm{CS}}}{S_{F,\mathrm{KH}}} \approx 7$. Assuming shot-noise-limited images, $\mathrm{SNR_{CS}} \approx 3 \times \mathrm{SNR_{KH}}$ which is close (given the many approximations embedded in Eq. 14) to the ≈5× gain in detection limit we report here. That said, pumping weaker absorption bands with higher powers does have several advantages including reduced degradation of laser power across the PLIF volume, ability to

use shorter exposure times, and reduced need to purge the beam path.

8 Conclusions

Scanned-wavelength IR-LIF and IR-PLIF techniques for spatially resolved imaging of temperature, pressure, and CO_2 mole fraction have been presented and demonstrated. These methods use a quantum-cascade laser with up to 120 mW of power to directly excite the ν_3 fundamental-vibration band of CO_2 for 200 to 10^5 times more absorbance than past IR-LIF and IR-PLIF work done with CO_2. LIF measurements of temperature, pressure, and CO_2 mole fraction within 2 % of known values were obtained by scanning the laser across two CO_2 absorption transitions and least-squares fitting a Voigt profile to the two transitions. Two-dimensional measurements of CO_2 and pressure were also demonstrated in CO_2–argon jets using IR-PLIF. In addition, simplified and detailed kinetic models were presented to enable quantitative, calibration-free measurements of CO_2 via LIF. As a result, this technique shows potential for studying a variety of applications with non-uniform composition (assuming differences in species-specific broadening and quenching are minor as is the case here) and pressure fields, with possible extension to imaging temperature and velocity.

Acknowledgments This work was supported by Air Force Office of Scientific Research under the Basic Research Initiative Program Grant Number FA9550-12-1-0472 with Dr. Chiping Li as Program Manager. The authors would like to thank Vince Morton and Todd Rumbaugh of Hadland Imaging and Frédérick Marcotte and Alexandrine Huot of Telops for demonstrating and operating the infrared camera.

References

1. R.B. Miles, E. Udd, M. Zimmermann, Quantitative flow visualization in sodium vapor seeded hypersonic helium. Appl. Phys. Lett. **32**, 317–319 (1978)
2. E.C. Rea, R.K. Hanson, Rapid laser-wavelength modulation spectroscopy used as a fast temperature measurement technique in hydrocarbon combustion, Appl. Opt. **27**, 4454–4464 (1988)
3. A.Y. Chang, B.E. Battles, R.K. Hanson, Simultaneous measurements of velocity, temperature, and pressure using rapid CW wavelength-modulation laser-induced fluorescence of OH. Opt. Lett. **15**, 706–708 (1990)
4. J. Hult, I.S. Burns, C.F. Kaminski, Measurements of the indium hyperfine structure in an atmospheric-pressure flame by use of diode-laser-induced fluorescence. Opt. Lett. **29**, 827–829 (2004)
5. I.S. Burns, C.F. Kaminski, Diode laser induced fluorescence for gas-phase diagnostics. Z. Phys. Chem. **225**, 1343–1366 (2011)
6. G. Kychakoff, R.D. Howe, R.K. Hanson, J.C. McDaniel, Quantitative visualization of combustion species in a plane. Appl. Opt. **18**, 3225–3227 (1982)
7. M.J. Dyer, D.R. Crosley, Two-dimensional imaging of OH laser-induced fluorescence in a flame. Opt. Lett. **8**, 382–384 (1982)
8. G. Kychakoff, R.D. Howe, R.K. Hanson, M.C. Drake, R.W. Pitz, M. Lapp, C.M. Penney, Science **224**, 382–384 (1984)
9. C. Schulz, V. Sick, Tracer-LIF diagnostics: quantitative measurement of fuel concentration, temperature and fuel/air ratio in practical combustion systems. Prog. Energy Combust. Sci. **31**, 75–121 (2005)
10. W.D. Kulatilaka, S.V. Naik, R.P. Lucht, Development of high-spectral-resolution planar laser-induced fluorescence imaging diagnostics for high-speed gas flows. AIAA J. **46**, 17–20 (2008)
11. Ronald K. Hanson, Applications of quantitative laser sensors to kinetics, propulsion and practical energy systems. Proc. Combust. Inst. **33**, 1–40 (2011)
12. B.J. Kirby, R.K. Hanson, Planar laser-induced fluorescence imaging of carbon monoxide using vibrational (infrared) transitions. Appl. Phys. B **69**, 505–507 (1999)
13. B.J. Kirby, R.K. Hanson, Imaging of CO and CO_2 using infrared planar laser-induced fluorescence. Proc. Combust. Inst. **28**, 253–259 (2000)
14. B.J. Kirby, R.K. Hanson, CO_2 imaging with saturated planar laser-induced vibrational fluorescence. Appl. Opt. **40**, 6136–6144 (2001)
15. D.A. Rothamer, R.K. Hanson, Temperature and pressure imaging using infrared planar laser-induced fluorescence. Appl. Opt. **49**, 6436–6447 (2010)
16. Z.T. Alwahabi, J. Zetterberg, Z.S. Li, M. Alden, High resolution polarization spectroscopy and laser induced fluorescence of CO_2 around 2 μm. Eur. Phys. J. D **42**, 41–47 (2007)
17. J. Zetterberg, S. Blomberg, J. Gustafson, Z.W. Sun, Z.S. Li, E. Lundgren, M. Aldén, An in situ set up for the detection of CO_2 from catalytic CO oxidation by using planar laser-induced fluorescence. Rev. Sci. Instrum. **83**, 053104 (2012)
18. H. Li, R.K. Hanson, J.B. Jeffries, H. Li, R.K. Hanson, J.B. Jeffries, Meas. Sci. Technol. **15**, 1285–1290 (2004)
19. L.S. Rothman, I.E. Gordon, Y. Babikov, A. Barbe, D. Chris Benner, P.F. Bernath, M. Birk, L. Bizzocchi, V. Boudon, L.R. Brown, A. Campargue, K. Chance, E.A. Cohen, L.H. Coudert, V.M. Devi, B.J. Drouin, A. Fayt, J.-M. Flaud, R.R. Gamache, J.J. Harrison, J.-M. Hartmann, C. Hill, J.T. Hodges, D. Jacquemart, A. Jolly, J. Lamouroux, R.J. Le Roy, G. Li, D.A. Long, O.M. Lyulin, C.J. Mackie, S.T. Massie, S. Mikhailenko, H.S.P. Müller, O.V. Naumenko, A.V. Nikitin, J. Orphal, V. Perevalov, A. Perrin, E.R. Polovtseva, C. Richard, M.A.H. Smith, E. Starikova, K. Sung, S. Tashkun, J. Tennyson, G.C. Toon, VlG Tyuterev, G. Wagner, The HITRAN2012 molecular spectroscopic database. J. Quant. Spectrosc. Radiat. Trans. **130**, 4–50 (2013)
20. B.J. Kirby, Infrared planar laser-induced fluorescence imaging and applications to imaging of carbon monoxide and carbon dioxide, PhD Thesis, Stanford University (2001)
21. R.M. Spearrin, W. Ren, J.B. Jeffries, R.K. Hanson, Multi-band infrared CO_2 absorption sensor for sensitive temperature and species measurements in high-temperature gases. Appl. Phys. B **116**, 855–865 (2014)
22. Christopher S. Goldenstein, Jay B. Jeffries, Ronald K. Hanson, Diode laser measurements of linestrength and temperature-dependent lineshape parameters of H_2O-, CO_2-, and N_2-perturbed H_2O transitions near 2474 and 2482 nm. J. Quant. Spectrosc. Radiat. Trans. **130**, 100–111 (2013)
23. D.C. Allen, T.J. Price, C.J.S.M. Simpson, Vibrational deactivation of the bending mode of CO_2 measured between 1500 K and 150 K, Chem. Phys. Lett. **45**, 183–187 (1976)
24. G.D. Billing, Semiclassical calculation of energy transfer in polyatomic molecules. VII. Intra- and inter-molecular energy transfer in $N_2 + CO_2$. Chem. Phys. **67**, 35–47 (1981)